

FAST RADIAL FLOWS IN TRANSITION DISK HOLES

Katherine A. Rosenfeld¹, Eugene Chiang², and Sean M. Andrews¹

ABSTRACT

Protoplanetary “transition” disks have large, mass-depleted central cavities, yet also deliver gas onto their host stars at rates comparable to disks without holes. The paradox of simultaneous transparency and accretion can be explained if gas flows inward at much higher radial speeds inside the cavity than outside the cavity, since surface density (and by extension optical depth) varies inversely with inflow velocity at fixed accretion rate. Radial speeds within the cavity might even have to approach free-fall values to explain the huge surface density contrasts inferred for transition disks. We identify observational diagnostics of fast radial inflow in channel maps made in optically thick spectral lines. Signatures include (1) twisted isophotes in maps made at low systemic velocities and (2) rotation of structures observed between maps made in high-velocity line wings. As a test case, we apply our new diagnostic tools to archival ALMA data on the transition disk HD 142527, and uncover evidence for free-fall radial velocities inside its cavity. Although the observed kinematics are also consistent with a disk warp, the radial inflow scenario is preferred because it predicts low surface densities that appear consistent with recent observations of optically thin CO isotopologues in this disk. How material in the disk cavity sheds its angular momentum wholesale to fall freely onto the star is an unsolved problem; gravitational torques exerted by giant planets or brown dwarfs are briefly discussed as a candidate mechanism.

Subject headings: accretion, accretion disks — planetary systems: protoplanetary disks — stars: pre-main sequence

1. INTRODUCTION

A subset of T Tauri and Herbig Ae disks have large, mass-depleted cavities in their inner regions, as inferred from their infrared spectra (e.g., Kim et al. 2013) or spatially resolved imaging at infrared (e.g., Geers et al. 2007) and mm wavelengths (e.g., Brown et al. 2009). The cavities in these “transition” disks have radii ranging from ~ 4 AU (TW Hya; Calvet et al. 2002; Hughes et al. 2007) to 20 AU (GM Aur; Hughes et al. 2009) to 40–50 AU (LkCa 15; Andrews et al. 2011; Isella et al.

¹Harvard-Smithsonian Center for Astrophysics, 60 Garden Street, Cambridge, MA 02138, USA

²Departments of Astronomy and Earth and Planetary Science, University of California, Berkeley, CA 94720, USA

2012) to 130–140 AU (HD 142527; Casassus et al. 2013). The suspicion is that dynamical interactions with nascent planetary systems evacuate the inner disk regions (e.g., Zhu et al. 2011).

Surprisingly, despite their optically thin cavities, many transition disks appear to be accreting gas at fairly normal rates. Stellar accretion rates \dot{M}_* in transition disks range from $\sim 10^{-9} M_\odot \text{yr}^{-1}$ (TW Hya; Muzerolle et al. 2000) to $10^{-8} M_\odot \text{yr}^{-1}$ (GM Aur; Gullbring et al. 1998; Calvet et al. 2005) to $10^{-7} M_\odot \text{yr}^{-1}$ (HD 142527; Garcia Lopez et al. 2006). These rates overlap with those for conventional disks without cavities, although the median \dot{M}_* for transitional disks may be a factor of ~ 10 lower than for conventional disks (Najita et al. 2007; Espaillat et al. 2012; Kim et al. 2013).¹

It is sometimes thought that transition disk cavities are created by planets consuming material from the outer disk and thereby starving the inner disk. This is unlikely to be correct — or at least it cannot be the whole story — because a starved inner disk would also starve the host star, contrary to the observed values of \dot{M}_* cited above. Modeling of disk spectra and images reveals that surface density contrasts inside and outside cavities can be $\gtrsim 10^3$ (e.g., Calvet et al. 2005). Planets inside the cavity cannot simultaneously eat $\gtrsim 99.9\%$ of the mass flowing inward from the outer disk and still leave enough for their host star to accrete at near-normal rates. If we interpret the factor-of-10 lower \dot{M}_* for transition disks as arising from planets consuming $\sim 90\%$ of the accretion flow from the outer disk and leaving the remaining $\sim 10\%$ for the central star (e.g., Lubow & D’Angelo 2006), then the surface density just inside the planet’s orbit would decrease by only a factor of 10, which is almost certainly too small to render the inner disk optically thin — all other factors being equal.

In this paper, we describe a way for transition disks to have their cake (possess optically thin cavities) and eat it too (accrete at normal rates). The dilemma can be resolved by (somehow) increasing the radial accretion velocity v_R inside the cavity, thereby concomitantly lowering the surface densities Σ there. For a given radius R and steady disk accretion rate $\dot{M} = 2\pi R\Sigma v_R$, we have $\Sigma \propto 1/v_R$. Just outside the cavity, Σ is large because accretion in the outer disk is diffusive (“viscous”) and slow ($v_R \sim \alpha(H/R)^2 v_K \ll v_K$, where H is the disk vertical thickness, $\alpha \ll 1$ is the Shakura-Sunyaev stress parameter, and v_K is the Keplerian orbital velocity). Just inside the cavity, the accretion velocity v_R is somehow boosted — v_R could, in principle, approach its maximum of $\sim v_K$ — so that Σ is lowered, conceivably by orders of magnitude, while maintaining the same mass flow rate \dot{M} as in the outer disk.

Gravitational (as opposed to magnetic or hydrodynamic) torques are an obvious candidate for catastrophically removing angular momentum from gas inside the cavity. In galaxies, gravitational

¹Of course, there are disks, transitional and otherwise, with lower accretion rates than those cited in the main text (e.g., Sicilia-Aguilar et al. 2010; Rigliaco et al. 2012)—at least insofar as attempts to measure accretion rates can be trusted (e.g., De Marchi et al. 2010; Curran et al. 2011; Alcalá et al. 2013). Some transitional disks with unmeasurably low stellar accretion rates may harbor stellar binaries whose torques are strong enough to stave off accretion (e.g., CoKu Tau/4; Ireland & Kraus 2008; Najita et al. 2007). Our focus in this paper is on healthily accreting transitional disks, as they pose the greatest paradox: how can they have cavities and accrete at the same time?

torques are exerted by stars that arrange themselves into non-axisymmetric patterns. A stellar bar (a perturbation with azimuthal wavenumber $m = 2$) eviscerates the interior of the ~ 3 -kpc molecular ring at the center of our Galaxy (Schwarz 1981; Binney et al. 1991); an eccentric stellar disk ($m = 1$) may be funneling gas onto the star-forming nucleus of M31 (Chang et al. 2007); and a complex nest of $m = 1$ and $m = 2$ stellar potentials force-feeds gas onto quasars (Shlosman et al. 1989; Hopkins & Quataert 2011). In these galaxy-scale examples, radial inflow velocities can approach free-fall rates.

The role of stars in galaxies might be played by planets in transition disks. We like this interpretation, but it is not without difficulty. The cavities are so large (they are not annular gaps) and so clean that appeals are made to rather extreme parameters. As many as four planets, each weighing up to $\sim 10 M_{\text{Jup}}$, have been posited to carve out a given cavity (Zhu et al. 2011; Dodson-Robinson & Salyk 2011).² At least in the case of the transition disk around LkCa 15, there might be one (but so far only one) actively accreting super-Jovian planet located well inside the disk cavity (Kraus & Ireland 2012). Some assistance in driving the accretion flow inside the cavity may be obtained from the gravitational potential of the outer disk itself, if that disk is sufficiently clumpy and massive (for examples of clumpy disks, see the observations of IRS 48 by van der Marel et al. 2013, and the studies of HD 142527 by Casassus et al. 2013 and Fukagawa et al. 2013). Just inside a non-axisymmetric outer disk, gas streamlines can cross, shock, and plunge inward (e.g., Paczynski 1977).

Disk radial velocities driven by embedded massive planets or brown dwarfs can be healthy fractions of orbital (azimuthal) velocities. We derive a crude estimate³ for v_R by equating the one-sided Lindblad torque — the amount of angular momentum transmitted outward across a planet’s orbit (Goldreich & Tremaine 1980) — with the angular momentum advected inward by accretion, $\dot{M}v_K R$. This balance yields

$$v_R \sim \left(\frac{M_p}{M_*}\right)^2 \left(\frac{R}{H}\right)^3 v_K \quad (1)$$

where we have used the total linear Lindblad torque, integrated over all resonances outside the torque cut-off zone at distances $\gtrsim H$ away from the planet (see, e.g., Goodman & Rafikov 2001 or Crida et al. 2006, and references therein). For a planet mass $M_p \sim 10 M_{\text{Jup}}$, a host stellar mass $M_* \sim 1 M_\odot$, and a typical disk aspect ratio $H/R \sim 0.1$, equation (1) evaluates to

$$v_R \sim 0.1 v_K \sim 0.5 \left(\frac{30 \text{ AU}}{R}\right)^{1/2} \text{ km s}^{-1}. \quad (2)$$

Modern heterodyne receivers on (sub)millimeter wavelength interferometers routinely observe disks

²Even multiple super-Jovian planets are reportedly not enough: grain growth and dust filtration at the cavity rim are invoked in addition to planets to make the cavity sufficiently transparent (Zhu et al. 2011; Dong et al. 2012).

³Our “zero-dimensional” analysis ignores the fact that actual disk flows around planets are two-dimensional and dominated by non-axisymmetric streams flowing in and around planetary Hill spheres. Still, some indirect empirical support for the scalings in equation (1) has been found by Fung et al. (2013).

at $\sim 0.1 \text{ km s}^{-1}$ resolution, and the Atacama Large Millimeter Array (ALMA) is expected to provide high sensitivity data at finer velocity scales yet. Evidence for free-fall radial velocities can be found in the HCO^+ filament within the disk cavity around HD 142527. Casassus et al. (2013) discovered this filament to be oriented nearly radially; in estimating \dot{M} for this system, they assumed $v_R \sim v_K$ (although the velocities of the HCO^+ filament were not actually quoted in their study).

Regardless of what is actually accelerating the accretion, we ask here whether we can test observationally the idea that transition disk cavities have fast (nearly free-fall) radial flows. We present in §2 some predicted observational signatures of radial inflow in spectrally and spatially resolved (sub)millimeter-wavelength maps of molecular emission lines. A sample case study based on the HD 142527 disk is presented in §3. We conclude in §4.

2. OBSERVATIONAL SIGNATURES OF RADIAL INFLOW

Interferometers observing the (sub)millimeter and radio spectral line transitions of molecular gas tracers produce a spatially resolved map of the source for each frequency (velocity) channel. A disk in Keplerian rotation has well-ordered gas velocities, and so line emission in a particular channel “highlights” disk material that is appropriately Doppler shifted (e.g., Omodaka et al. 1992; Beckwith & Sargent 1993). Adding a fast radial inflow to the normal Keplerian velocity field alters the morphology of channel map emission (cf. Tang et al. 2012). We identify two related observational signatures of radial inflow in a disk cavity: (1) twisted isophotes in the channel map corresponding to the systemic velocity (§2.1), and (2) rotation of features seen between maps made in high-velocity wings (§2.2). While distinctive, neither of these features is entirely unique, and must be disentangled from other non-Keplerian effects (§2.3).

Our analysis uses two axisymmetric models: a razor-thin disk and a three-dimensional (3D) disk. The razor-thin model is a pedagogical tool to develop intuition. The 3D model is more realistic and presents a platform to test the razor-thin model as well as analyze mock data products.

Both models treat the gas velocities within the cavity ($R < R_{\text{cav}}$) as having an inward radial component that is some constant fraction χ of the local circular Keplerian velocity. The velocity field is then

$$v_x = -v_K \sin \theta - \chi v_K \cos \theta \tag{3}$$

$$v_y = +v_K \cos \theta - \chi v_K \sin \theta, \tag{4}$$

both for the razor-thin model and the 3D model. Here θ is the azimuthal angle in the disk plane, and variations in bulk velocity with height z are ignored (but see §2.3). Outside the cavity, gas is assumed to follow circular Keplerian orbits. Our assumption that the radial inflow is axisymmetric is probably unrealistic — certainly so if the inflow is driven by large-scale gravitational torques as we have described in §1. Nevertheless we assume axisymmetry to gain a foothold on the problem.

The disk is inclined by a viewing angle i about the x axis, where $i = 0^\circ$ corresponds to a disk

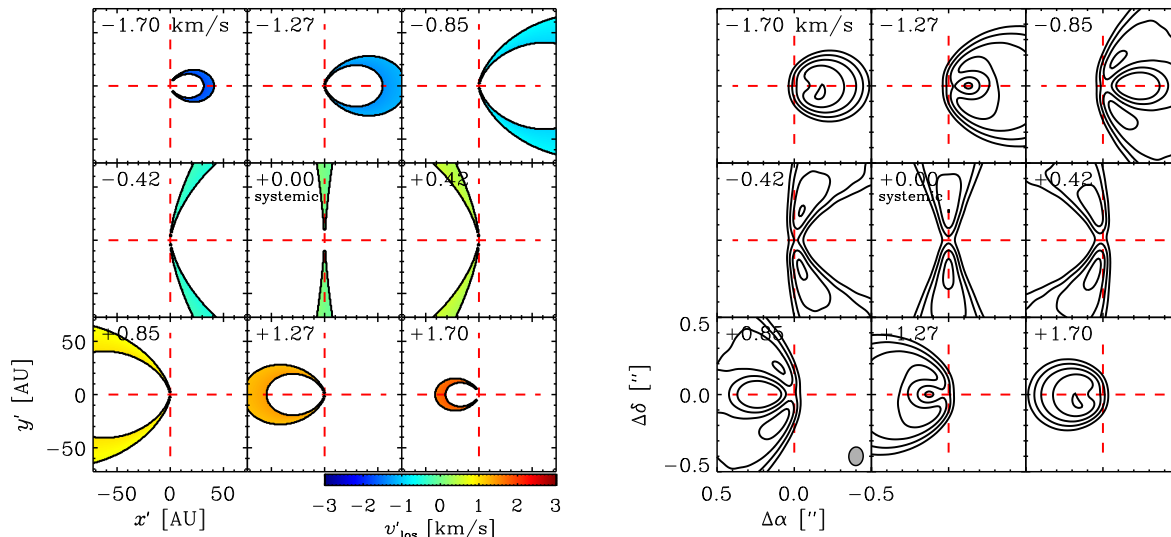


Fig. 1.— *Left*: Regions of a razor-thin disk model ($i = 20^\circ$, $\chi = 0$) where the velocities v'_{los} fall within each labeled spectral channel of width $\Delta v'_{\text{los}} = \pm 0.212 \text{ km s}^{-1}$. *Right*: Simulated $^{12}\text{CO } J=3-2$ channel maps for a 3D disk with the same i and χ . Projected major (horizontal) and minor (vertical) axes of the disk are shown as dashed red lines. The spatial scales of all panels are identical for a distance of 145 pc. The morphology of line emission in the channel maps (right) respects the velocity field (left). The synthesized beam for the simulated 3D model is $0''.12 \times 0''.09$, with the beam major axis oriented at position angle $\text{PA} = -3^\circ$.

seen face-on. Note that the effects we will discuss are sensitive to the spin orientation of the disk, and so i can range between 0° and 180° without degeneracy. Inclinations $0^\circ < i < 90^\circ$ imply that the line-of-sight component of the orbital angular momentum points toward the observer, whereas $90^\circ < i < 180^\circ$ implies that the line-of-sight component points away.

For the razor-thin model, the projected line-of-sight velocity is⁴

$$v'_{\text{los}} = -v_y \sin i = -v_K \sin i \cos \theta + \chi v_K \sin i \sin \theta. \quad (5)$$

We utilize primed coordinates to denote values measured by the observer; the spatial coordinates in the sky plane are $x' = x$ and $y' = y \cos i$. The azimuth θ measured in the disk plane is related to the on-sky angle θ' by $\tan \theta' = \cos i \tan \theta$. The left panel of Figure 1 shows the morphology of line emission for a razor-thin disk with no inflow.

We compute an analogous 3D disk model that simulates the $^{12}\text{CO } J=3-2$ line emission from a disk with a total gas mass of $0.01 M_\odot$, a spatially constant $\text{CO}:\text{H}_2$ number-abundance fraction of

⁴We can set v'_{los} equal to either $+v_y \sin i$ or $-v_y \sin i$. The degeneracy arises because we can choose the disk's ascending (\equiv toward the observer) node on the sky plane to coincide with either the $x = x'$ axis (our convention in this paper) or the $-x = -x'$ axis. Another way to say this is that i is degenerate with $-i$.

10^{-4} , and a Gaussian vertical density distribution ($\exp(-z^2/2H^2)$ with a scale height of $H = 0.1R$). The surface density profile is that of a thin, viscously accreting disk (Lynden-Bell & Pringle 1974): $\Sigma \propto R^{-1} \exp(-R/R_s)$ with scale radius $R_s = 50$ AU and an outer truncation radius of 300 AU. Since our focus in this paper is on the velocity field and not on the density structure, we have not included any reduction of Σ within the cavity. This simplification should not introduce serious error as long as the cavity region remains optically thick in ^{12}CO emission—we estimate that this condition holds for $\dot{M} \gtrsim 10^{-8} M_\odot/\text{yr}$ and $R_{\text{cav}} \lesssim 50$ AU, even if χ jumps discontinuously from 0 to 1 across the cavity boundary. These requirements are satisfied for HD 142527, our subject test case of §3.

The model is vertically isothermal with a power-law radial temperature profile, $T(R) = 25(R/100 \text{ AU})^{-0.5}$ K: this temperature profile is used only to calculate the level populations of molecules, not the hydrostatic disk structure. The mass of the central star is $1 M_\odot$, the distance to the observer is 145 pc, and the cavity radius is $R_{\text{cav}} = 50$ AU. The disk inclination i and radial inflow parameter χ are variable. We use the modeling capabilities of LIME (Brinch & Hogerheijde 2010) to simulate high-resolution channel maps assuming LTE conditions and a turbulent linewidth of $\xi = 0.01 \text{ km s}^{-1}$. We then use CASA to sample and deconvolve the Hanning-smoothed visibilities with a spectral resolution of 0.212 km s^{-1} and a spatial resolution of $0''.1$: these parameters should typify spectral line observations of disks by ALMA when the instrument reaches technical maturity. The right panel of Figure 1 shows the channel maps from a 3D disk model ($\chi = 0$), zoomed into the inner $\pm 0''.5$. Comparing the left and right panels of Figure 1 reveals how the velocity field of the razor-thin model offers a guide to the morphology of line emission in the channel maps of the 3D model (see also Beckwith & Sargent 1993).

2.1. Twisted Isophotes at the Systemic Velocity

The gas with no bulk motion relative to the systemic velocity of the disk has $v'_{\text{los}} = 0$. From equation (5), this gas satisfies

$$0 = -v_K \sin i \cos \theta_{\text{sys}} + \chi v_K \sin i \sin \theta_{\text{sys}}, \quad (6)$$

which implies that $\theta_{\text{sys}} = \arctan(\chi^{-1})$ in the disk plane, and $\theta'_{\text{sys}} = \arctan(\chi^{-1} \cos i)$ on the sky. For $\chi = 0$ (no radial inflow), $\theta'_{\text{sys}} = 90^\circ$: the systemic velocity channel probes gas that lies along the minor axis of the disk as seen in projection (see Figure 1, central panels). When $\chi \neq 0$, the isovelocity contours at $v'_{\text{los}} = 0$ will be rotated by an angle $\Delta\theta'_{\text{sys}} = \theta'_{\text{sys}} - 90^\circ$. This rotation is evident in the top set of panels in Figure 2, which show the line-of-sight velocity fields of a razor-thin disk for various values of χ inside the disk cavity. The rotation can also be seen in the isophotes observed at the systemic velocity of the corresponding 3D model; the bottom panels of Figure 2 show that the isophotes in the channel maps “twist” at $R = R_{\text{cav}}$.

The isophote twist in the systemic velocity channel map can be measured as a function of radius. We perform this measurement by first dividing the 3D disk model into concentric annuli,

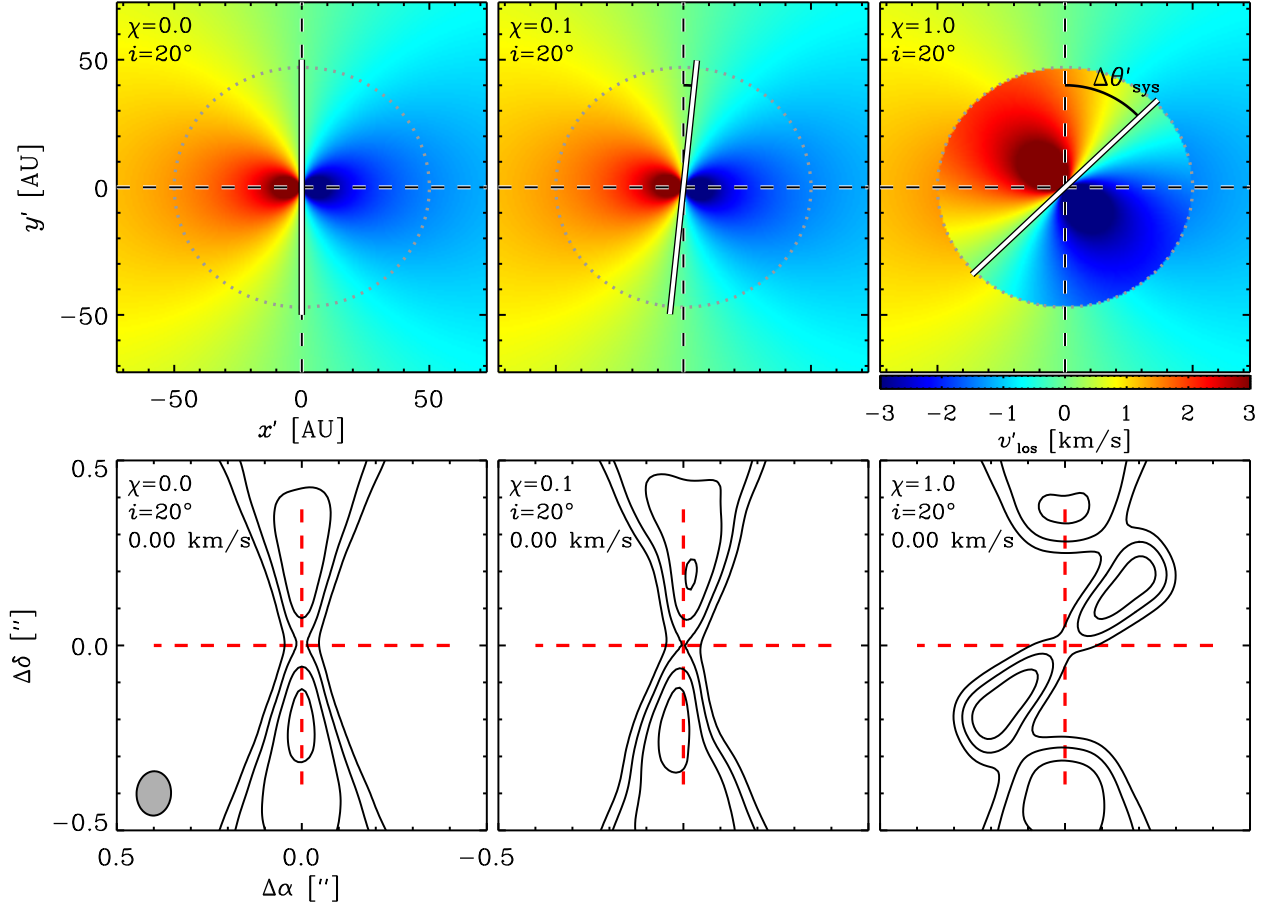


Fig. 2.— Twisted isophotes at the systemic velocity. *Top*: Observed velocity fields v'_{los} for razor-thin disks with varying degrees of radial inflow. Within the cavity radius $R_{\text{cav}} = 50$ AU, gas flows axisymmetrically inward with a velocity χ times the local circular Keplerian velocity. The dotted gray circle traces the cavity boundary, the solid white bar indicates θ'_{sys} , and the black arc traces $\Delta\theta'_{\text{sys}} = \theta'_{\text{sys}} - 90^\circ$. Dashed lines show the projected major (horizontal) and minor (vertical) axes. *Bottom*: Simulated channel maps at the systemic velocity for 3D disks having the same i and χ as the razor-thin models shown in the top panels. The isophotes twist at the location of the cavity radius ($\sim 0''.34$ from the map centers).

and further splitting each annulus into its top ($y' > 0$) and bottom ($y' < 0$) halves. For each half-annulus, an intensity-weighted centroid (i.e., a “center of brightness”) is computed. The rotation angle $\Delta\theta'_{\text{sys}}$ is then evaluated from the line joining the centroid positions of the top and bottom halves of a given annulus at radius R . The left panel of Figure 3 shows $\Delta\theta'_{\text{sys}}(y')$ for three values of χ . Note how $\max|\Delta\theta'_{\text{sys}}|$ is accurately predicted by the razor-thin model, at least for the example inclination angle $i = 20^\circ$. In the mock observations of the 3D model, the transition between $\Delta\theta'_{\text{sys}} = 0$ and $\max|\Delta\theta'_{\text{sys}}|$, occurring near the cavity radius ($R_{\text{cav}} = 50$ AU), is smeared by the $0''.1$

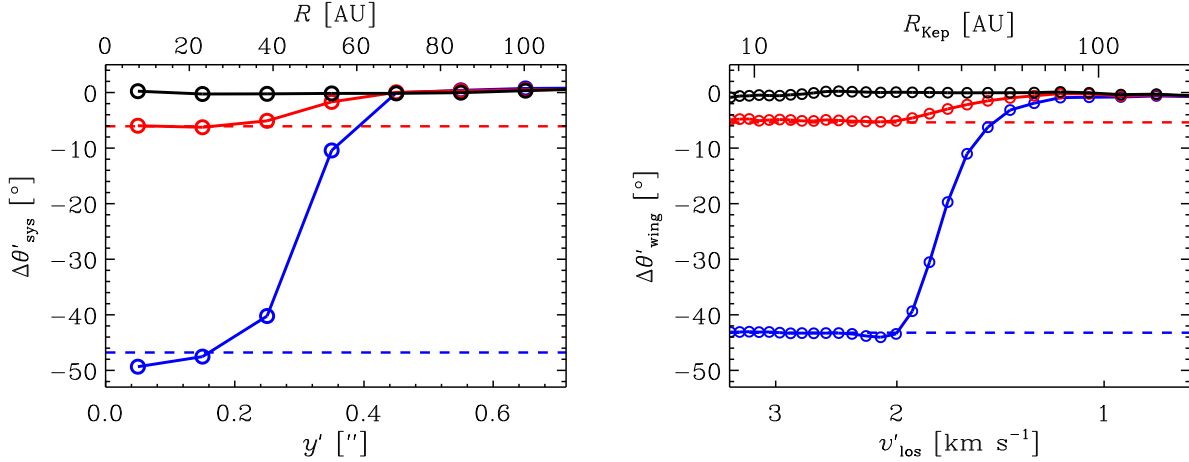


Fig. 3.— Rotation angles $\Delta\theta'_{\text{sys}}$ (*left*) and $\Delta\theta'_{\text{wing}}$ (*right*) for $\chi = 0$ (black), 0.1 (red), and 1 (blue) in 3D disk models with $i = 20^\circ$ and $R_{\text{cav}} = 50$ AU. $\Delta\theta'_{\text{sys}}$ is measured in the systemic velocity channel ($v'_{\text{los}} = 0$) as a function of radius, and $\Delta\theta'_{\text{wing}}$ is derived against channel velocity. Analytic predictions from razor-thin disk models are drawn with horizontal dashed lines. The lower abscissa of the left panel plots projected distance along the disk’s major axis, while the upper abscissa of the right panel plots the radius for which $v_{\text{K}} \sin i = v'_{\text{los}}$.

beam. How well we can measure $\Delta\theta'_{\text{sys}}$ in practice depends on the ratio of the beam size, θ_{beam} , to the peak signal-to-noise, S/N (Reid et al. 1988). We estimate that a robust measurement of the twist requires $\theta_{\text{beam}} \lesssim (S/N) |(R_{\text{cav}}/d) \sin i \tan \Delta\theta'_{\text{sys}}|$. For the $0''.1$ beam size adopted in Figure 3, this requirement is met with $S/N > 10$ for $\chi = 0.1$, or with any detection of the line for $\chi = 1$. Any measurement of an isophote twist from a synthesized image should be accompanied by a model imaged using the same u, v sampling as the data, since the position angle of the resolution element can significantly alter the appearance of the image (Guilloteau & Dutrey 1998).

2.2. Maximum LOS Velocities: Wing Rotation

We now consider gas moving at the highest line-of-sight velocities, responsible for emission in the spectral line wings. Maximizing equation (5) with respect to θ yields

$$0 = v_{\text{K}} \sin i \sin \theta_{\text{wing}} + \chi v_{\text{K}} \sin i \cos \theta_{\text{wing}}, \quad (7)$$

or $\theta_{\text{wing}} = \arctan(-\chi)$ in the disk plane and $\theta'_{\text{wing}} = \arctan(-\chi \cos i)$ on the sky. Radial inflow causes the maximum isovelocity contour to rotate away from the disk major axis by $\Delta\theta'_{\text{wing}} = \theta'_{\text{wing}}(\chi) - \theta'_{\text{wing}}(\chi = 0) = \theta'_{\text{wing}}(\chi)$. Figure 4 shows the velocity fields for three razor-thin disk models, together with simulated channel maps for the corresponding 3D models. Where there is inflow, emission from the 3D model is systematically rotated away from the disk major axis. For extreme values of $\chi \sim 1$, line-of-sight velocities within the cavity are noticeably greater than for

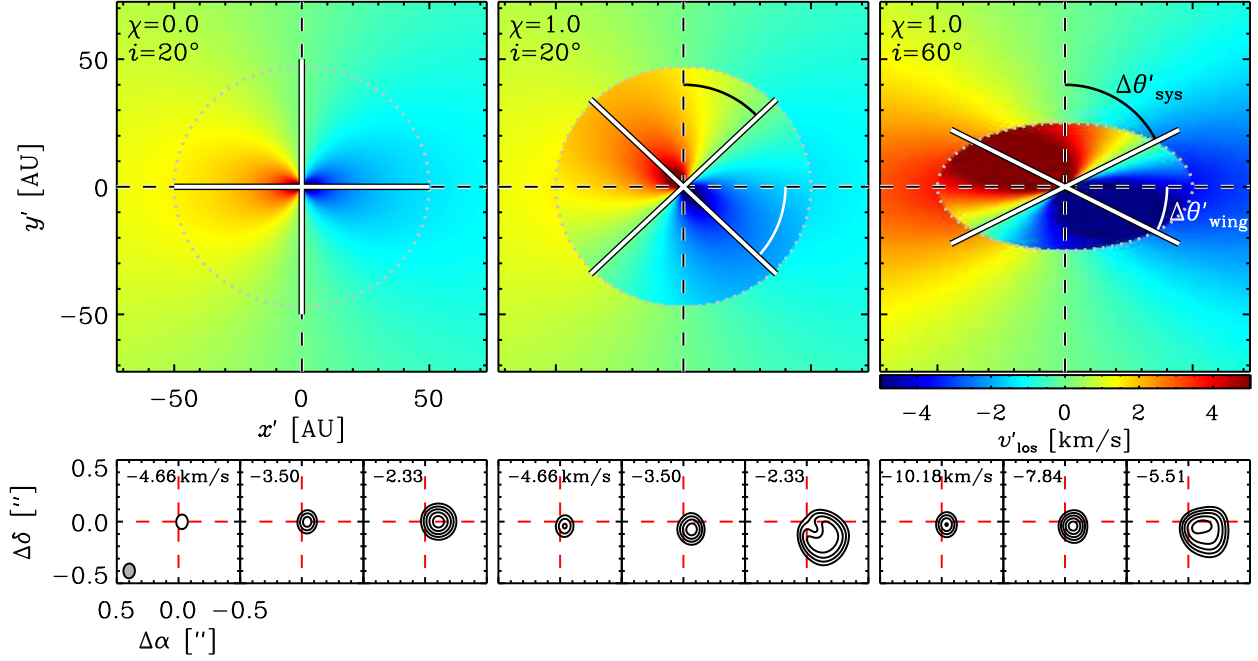


Fig. 4.— Wing rotation. *Top*: Rotation angles $\Delta\theta'_{\text{wing}}$ (white arcs), overlaid on velocity fields of razor-thin disk models. Other symbols are the same as in Figure 2. Note how $\Delta\theta'_{\text{wing}} \neq \Delta\theta'_{\text{sys}}$. *Bottom*: Simulated channel maps for various line-of-sight velocities from corresponding 3D disk models. Comparison of $\chi = 0$ with $\chi = 1$ shows how wing emission brightens and rotates clockwise from the projected major axis.

the case with no inflow (see top panels of Figure 4). Correspondingly, emission from the line wings is brighter — compare channels of the same velocity between the $\chi = 0$ and $\chi = 1$ models at fixed $i = 20^\circ$ (bottom panels of Figure 4) — although it should be remembered that any decrease in the surface density inside the cavity (not modeled here) may reduce the intensity enhancement. The last panel of Figure 4 demonstrates that $\Delta\theta'_{\text{wing}} \neq \Delta\theta'_{\text{sys}}$. This difference is further quantified in Figure 5, which shows that $|\Delta\theta'_{\text{wing}} - \Delta\theta'_{\text{sys}}|$ increases with increasing i and χ . Note how $|\Delta\theta'_{\text{wing}}|$ is reduced for highly inclined disks, just opposite to the behavior of $|\Delta\theta'_{\text{sys}}|$. Therefore, measuring $\Delta\theta'_{\text{wing}}$ is easier at low inclinations, while measuring $\Delta\theta'_{\text{sys}}$ is easier at high inclinations. Clearly, disk orientation is a consideration when designing observations to detect either rotational signature.

To measure $\Delta\theta'_{\text{wing}}$ for the 3D disk model, we employ a procedure similar to the one we devised for $\Delta\theta'_{\text{sys}}$. For each spectral channel, we measure the position of the intensity-weighted centroid (fitting two-dimensional Gaussians produces consistent results). Pairs of these positions are constructed from channels blue- and red-shifted by the same velocity relative to the systemic channel. For a given velocity pair, the angle $\Delta\theta'_{\text{wing}}$ is calculated from the line segment joining the two centroid positions. The second panel in Figure 3 shows $\Delta\theta'_{\text{wing}}$ as a function of channel velocity for a few values of χ . Rotation is evident for all channel velocities equal to the Kepler

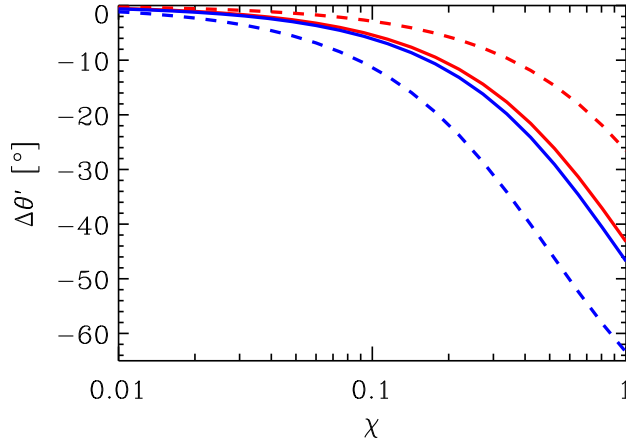


Fig. 5.— Rotation angles $\Delta\theta'_{\text{sys}}$ (blue) and $\Delta\theta'_{\text{wing}}$ (red) for razor-thin disk models as a function of the radial inflow parameter χ . Solid and dashed curves are for disk inclinations $i = 20^\circ$ and 60° , respectively. At fixed χ and i , $|\Delta\theta'_{\text{sys}}| > |\Delta\theta'_{\text{wing}}|$. Measuring $\Delta\theta'_{\text{wing}}$ is easier at low inclinations, while measuring $\Delta\theta'_{\text{sys}}$ is easier at high inclinations.

velocities of material within the cavity. As was the case for $|\Delta\theta'_{\text{sys}}|$, the maximum value of $|\Delta\theta'_{\text{wing}}|$ measured in the 3D model is accurately predicted by the razor-thin model. Measuring $|\Delta\theta'_{\text{wing}}|$ in practice requires $\theta_{\text{beam}}/(S/N) \lesssim |(R_{\text{cav}}/d) \sin i \tan \Delta\theta'_{\text{wing}}|$. For the model disks shown in Figure 4 with $\chi = 1$, this beam size requirement is met when $S/N \geq 5$ and with relatively large beam sizes, $<0''.5$ or $<0''.7$ for $i = 20^\circ$ or 60° , respectively.

In principle, the inclination i and inflow parameter χ can be calculated if both θ'_{sys} and θ'_{wing} are measured. In this case the product $\tan(\theta'_{\text{wing}}) \tan(\theta'_{\text{sys}}) = -\cos^2 i$ and the ratio $\tan(\theta'_{\text{wing}})/\tan(\theta'_{\text{sys}}) = -\chi^2$. The disk inclination so derived could then be compared to independent measurements.

These observational signatures of radial inflow — twisted isophotes ($\Delta\theta'_{\text{sys}}$) and wing rotation ($\Delta\theta'_{\text{wing}}$) — are intrinsically kinematic features, and therefore should be present regardless of which spectral line is used as a tracer of the projected disk velocity field. That said, there is an obvious advantage to using lines with higher optical depths (e.g., ^{12}CO , HCO^+), since they are more likely to be bright enough inside the low-density cavities of transitional disks (e.g., Bruderer 2013) to enable robust measurements of radial inflow.

2.3. Disentangling Radial Inflow from Other Non-Keplerian Effects

The rotational signatures of inflow identified in §2.1 and §2.2 can be mimicked to varying degrees by other phenomena. We discuss four possible “contaminants” and how one might disambiguate between these different scenarios.

2.3.1. Radial outflow

Molecular gas can be entrained in winds flowing up and radially outward from the disk surface (e.g., Pontoppidan et al. 2011; Bast et al. 2011; Klaassen et al. 2013). Radial outflow would cause the systemic velocity isophotes and the wing emission to rotate in the direction opposite to that for radial inflow. Distinguishing inflow from outflow requires that we resolve the spin orientation of the disk; i.e., we need to decide whether $i < 90^\circ$ or $i > 90^\circ$. The way to break this degeneracy is to use spatially resolved channel maps to decide which limb is approaching and which limb is receding, and then to combine this information with some asymmetry along the projected minor axis. The asymmetry could be manifested in the orientation of a polar jet pointed toward the observer (i.e., whether the jet points along the positive $y > 0$ or negative $y < 0$ minor axis). Alternatively, one could observe, at any wavelength, a spectral line (Dutrey et al. 1998; Guilloteau & Dutrey 1998; Rosenfeld et al. 2013) or continuum (Augereau et al. 1999; Weinberger et al. 1999; Fukagawa et al. 2006; Thalmann et al. 2010) brightness asymmetry arising from the disk’s orientation. Of course it is also possible that one molecular line traces an outflowing disk wind, say because it probes gas at high altitude above the midplane, while another traces radial inflow, closer to the midplane.

2.3.2. Infall from a molecular envelope

Gas from the parent molecular cloud may continue to accrete onto the protoplanetary disk at early times (Stahler et al. 1994; Yorke & Bodenheimer 1999; Brinch et al. 2007). Differential rotation and accelerating infall will mimic the spatio-kinematic signatures of inflow (cf. Brinch et al. 2008; Tang et al. 2012). However, the spatial scale of an infalling envelope should be comparable to or larger than the disk itself, and should not be confined to a central cavity. Furthermore, for an isolated source, the duration of infall should be considerably shorter than the lifetime of the disk (e.g., Piétu et al. 2005). Evidence for local cloud material might be indicated by high extinction values, very red infrared spectral energy distributions, or contamination (self-absorption and/or emission on much larger angular scales) in single dish molecular line spectra. Most of the currently known transition disks do not exhibit any clear evidence for a remnant envelope structure.

2.3.3. Vertical disk structure

Line emission from optically thick gas typically originates in disk surface layers located at large vertical heights above the midplane (e.g., van Zadelhoff et al. 2001; Dartois et al. 2003; Pavlyuchenkov et al. 2007; Semenov et al. 2008). Therefore, in channel maps, the blue- and red-shifted emission structures are not generally collinear with the stellar position; rather, they appear rotated away from the midplane in opposite directions from one another (Rosenfeld et al. 2013; de Gregorio-Monsalvo et al. 2013). These rotations of the blue- and red-shifted line wings would effectively cancel out in the procedure we developed in §2.2 to measure $\Delta\theta'_{\text{wing}}$. Moreover, vertical structure does not twist the

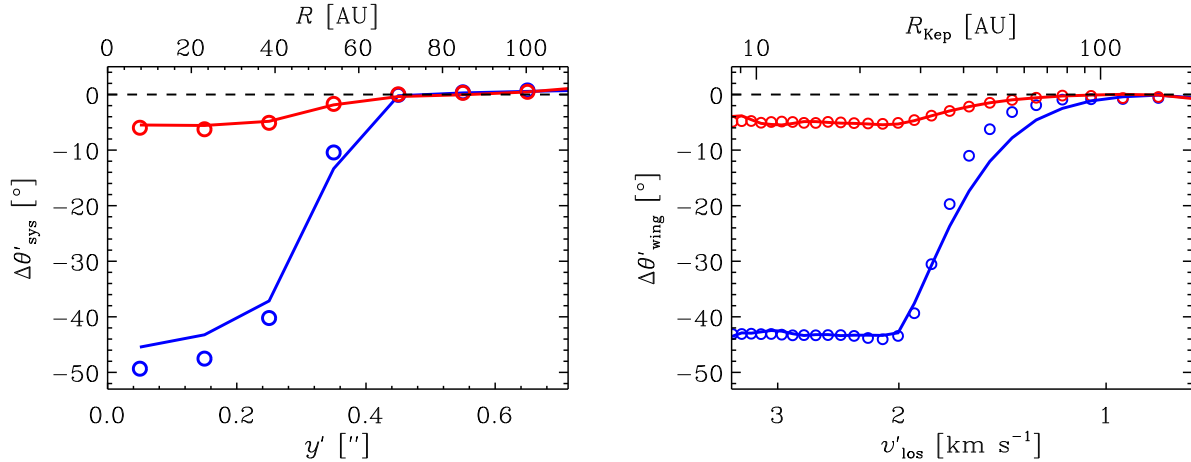


Fig. 6.— Degeneracy between a warp and radial inflow. The same rotation angles for inflow models as shown in Figure 3 are plotted here as open circles, and overlaid with solid curves generated from model warped disks. Warp parameters were chosen to reproduce $\Delta\theta'_{\text{wing}}$ for the inflow models; evidently these same warp models automatically mimic $\Delta\theta'_{\text{sys}}$ as well. For $\chi = 1$, the warp parameters are $R_w = R_{\text{cav}} = 50$ AU, $i_{\text{rel}} = 14^\circ$, and $\Omega_{\text{rel}} = 250^\circ$. For $\chi = 0.1$, $R_w = 50$ AU, $i_{\text{rel}} = 2^\circ$, and $\Omega_{\text{rel}} = 267^\circ$.

isophotes at the systemic velocity (i.e., $\Delta\theta'_{\text{sys}} = 0$). In sum, vertical structure should pose little danger of confusion in efforts to characterize radial inflow.

2.3.4. A warp

A warp — introduced, for example, by a perturbing body whose orbit is inclined to the disk plane (Larwood 1997; Marzari & Nelson 2009) — also changes the morphology of line emission in channel maps. We have found that, unfortunately, the warp-induced changes in the channel maps are practically identical to those induced by a radial inflow.⁵ At its most basic, a warp comprises an inner disk that is misaligned with an outer disk, and is described by three parameters: the radius R_w where the inner disk transitions to the outer disk, the inclination i_{inner} of the inner disk relative to the sky plane, and the orientation of the inner disk, i.e., the longitude Ω_{inner} of ascending (\equiv toward the observer) node, measured in the sky plane and referred to the $x = x'$ axis (as a reminder, the outer disk has inclination $i_{\text{outer}} \equiv i$ relative to the sky plane and orientation $\Omega_{\text{outer}} \equiv 0^\circ$). An equivalent description uses the outer disk as the reference plane; under this alternate convention, the inner disk inclination relative to the outer disk is i_{rel} , and its longitude of ascending node is Ω_{rel} , measured in the outer disk plane and referred to the $x = x'$ axis. The angles in the two reference

⁵We also tested whether disk eccentricity was degenerate with the signature of radial inflow, and found that it was not (data not shown).

systems are related by

$$i_{\text{rel}} = \arccos(\cos i \cos i_{\text{inner}} + \cos \Omega_{\text{inner}} \sin i \sin i_{\text{inner}}) \quad (8)$$

$$\Omega_{\text{rel}} = \frac{\pi}{2} + \arctan\left(\frac{\cos i_{\text{inner}} \sin i - \cos i \cos \Omega_{\text{inner}} \sin i_{\text{inner}}}{\sin i_{\text{inner}} \sin \Omega_{\text{inner}}}\right). \quad (9)$$

Figure 6 shows $\Delta\theta'_{\text{sys}}$ and $\Delta\theta'_{\text{wing}}$ for two 3D disk models with warps (solid curves) overlaid on our previous results for disk models with radial inflow (open circles). The similarity between these rotation angle patterns demonstrates that a warp with the right parameters (see caption) can masquerade as inflow in channel maps. Furthermore, increasing i_{rel} can brighten wing emission in the same way that increasing χ does (data not shown; see §2.2; Rosenfeld et al. 2012).

Distinguishing inflow from a warp requires additional data and modeling. A warped disk located in a region that is known to be optically thin at continuum wavelengths would need to have its opacity be reduced by large factors by, e.g., grain growth or dust filtration at the cavity rim. By contrast, in the fast inflow model, the opacity need not change much, if at all, since the surface density reduction that accompanies fast inflow would account for most if not all of the cavity’s transparency. Spatially resolved, multi-wavelength imaging of the disk cavity can serve to constrain changes in the dust size distribution. And one can utilize emission lines from rarer, optically thin gas species (e.g., Bruderer 2013) to measure total gas surface densities. In §3 we wrestle again with the warp/inflow degeneracy using real observations.⁶

3. A CASE STUDY: HD 142527

We consider the remarkable transition disk hosted by the young F star HD 142527. At a distance of $d = 145 \pm 15$ pc (Verhoeff et al. 2011), the disk has a large dust-depleted cavity of radius $R_{\text{cav}} \sim 130$ AU that has been imaged in near-infrared scattered light (Fukagawa et al. 2006; Casassus et al. 2012; Rameau et al. 2012; Canovas et al. 2013) and mid-infrared thermal emission (Fujiwara et al. 2006; Verhoeff et al. 2011). The cavity is not completely devoid of dust; Verhoeff et al. (2011) required an optically thick disk (and even an optically thin halo) interior to ~ 30 AU to explain the observed near-infrared and mid-infrared emission. ALMA Band 7 (345 GHz) observations presented by Casassus et al. (2013) resolved the highly asymmetric dust ring at R_{cav} that was originally noted by Ohashi (2008). The ALMA data clearly demonstrate that molecular gas resides inside the cavity, emitting in the $^{12}\text{CO } J=3-2$ and $\text{HCO}^+ J=4-3$ lines. We have already noted the nearly free-fall radial velocities implied by the HCO^+ filament (§1).

We apply the tools developed in §2 to the archival ALMA data on CO and HCO^+ line emission. We aim here only for a first look at the kinematics, and so forego an extensive modeling effort,

⁶A warp and inflow are not mutually exclusive possibilities — the two phenomena might be driven simultaneously by companions inside the disk cavity.

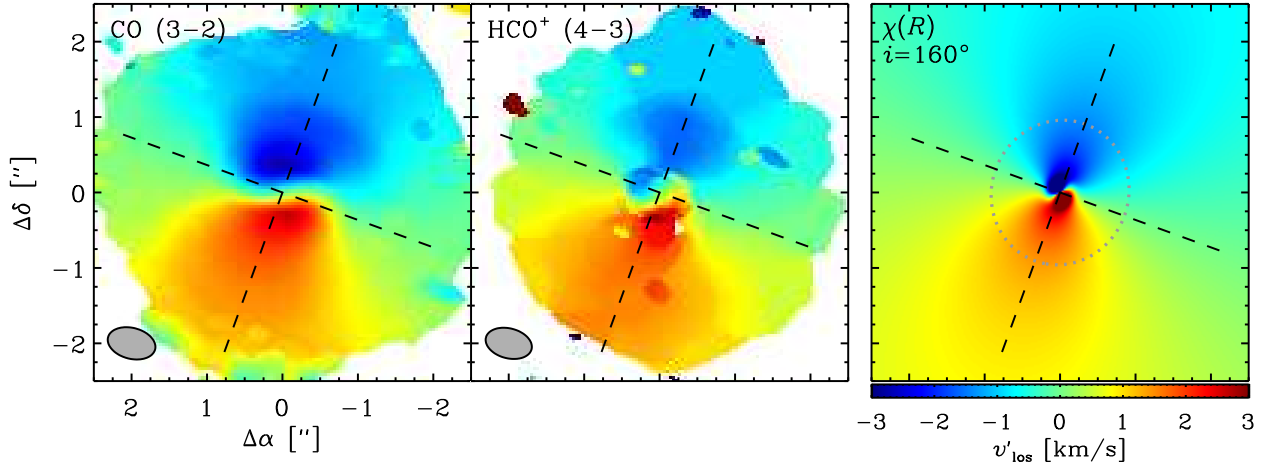


Fig. 7.— Evidence for fast radial inflow in the HD 142527 disk. *Left*: First moment or intensity-weighted velocity map of the ^{12}CO $J=3-2$ emission line constructed from archival ALMA data. *Center*: First moment map of the HCO^+ $J=4-3$ emission line. The HCO^+ data has lower signal-to-noise than the CO data. *Right*: Velocity field for a razor-thin disk with the inflow parameter χ increasing with decreasing R and peaking at unity (see text for details). All panels are colored using the same velocity scale, and the orientation of the outer disk is indicated by dashed black lines (projected major axis at $\text{PA} = -20^\circ$). The counter-clockwise twist, a signature of radial inflow for $i > 90^\circ$, is present in all panels; in the first moment maps, the twist appears on larger scales where the emission line intensity is strongest.

fixing in advance the disk mass ($0.1 M_\odot$), scale radius ($R_s = 50 \text{ AU}$), disk temperature ($T = 70(R/50 \text{ AU})^{-0.7} \text{ K}$), and outer truncation radius (300 AU). We also adopt literature values for the stellar mass ($M = 2.7 M_\odot$; Casassus et al. 2013) and viewing geometry for the outer disk ($i = 160^\circ$, with the projected major axis oriented at position angle $\text{PA} = -20^\circ$;⁷ Fujiwara et al. 2006; Verhoeff et al. 2011). The inclination and PA of the outer disk are based on CO channel maps together with thermal mid-infrared images which show that the eastern side of the disk appears brighter than the western side; on the eastern side we are seeing the portion of the cavity rim located farther from the observer and directly illuminated by starlight. The line-of-sight velocities reported below are all relative to systemic; the systemic velocity is $+3.64 \text{ km s}^{-1}$ relative to the local standard of rest, as we deduced from visual inspection of the CO channel maps.

Figure 7 shows the first moment maps for the CO and HCO^+ emission lines. The first moment or intensity-weighted line-of-sight velocity appears twisted near the disk center ($R' \lesssim 0''.5$). With respect to the orientation defined by the outer disk, the twist in the inner disk is counter-clockwise, which given $i = 160^\circ$ implies radial inflow. Furthermore, the twist is of order ~ 1 radian in magnitude, which implies a radial speed comparable to Keplerian ($\chi \sim 1$). Compare the first moment

⁷Alternatively, if our x' -axis points west and our y' -axis points north, then $\Omega_{\text{outer}} = 70^\circ$.

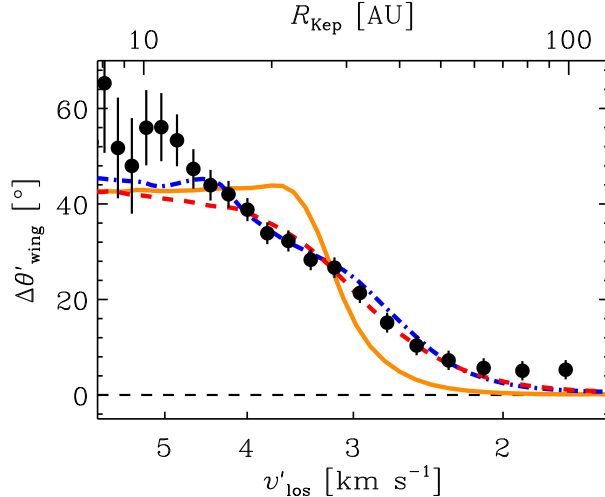


Fig. 8.— Possible fast inflow in the HD 142527 disk. The measured rotation, $\Delta\theta'_{\text{wing}}$, in the ^{12}CO $J=3-2$ line wings can be approximately reproduced by either a disk with graded radial inflow (spatially variable χ ; red dashed curve), or a graded warp (spatially variable i_{rel} and Ω_{rel} ; blue dot-dashed curve). Details of the models are in the main text. An inflow model having constant $\chi = 1$ for $R < 35$ AU (orange) does less well than the graded inflow model. The spin orientation of the HD 142527 disk ($i = 160^\circ$) is opposite to those of our example disks (having $i < 90^\circ$) in §2, and so $\Delta\theta'_{\text{wing}}$ is positive rather than negative.

maps (left and center panels) with the velocity field of a model razor-thin disk with a fast inflow (right panel; cf. Figure 4), and recognize that the comparison is only meant to be suggestive since the velocity field is not the same as the intensity-weighted velocity.

Figure 8 compares the measured $\Delta\theta'_{\text{wing}}(v'_{\text{los}})$ in the CO line with predictions from several models. A constant χ model does not fit the data as well as a variable $\chi(R < 140 \text{ AU} = [1 + (R/33 \text{ AU})^6]^{-1})$ model that introduces the twist incrementally. The variable χ model does as well as a warped disk model (cf. §2.3.4) in which the warp is likewise introduced gradually. To mock up a warp induced by a planet as described by linear secular theory (e.g., Dawson et al. 2011), we ramp up the relative inclination linearly from 0 to its final value $i_{\text{rel}} = 15^\circ$, and ramp down the nodal angle linearly from $\Omega_{\text{rel}} + 90^\circ$ to $\Omega_{\text{rel}} = 69^\circ$, as the disk radius decreases from $2R_w$ to $R_w = 25$ AU.

At the highest velocities/smallest radii probed in Figure 8, all our models systematically underpredict $\Delta\theta'_{\text{wing}}$. For the inflow model, the fit at small radii could be improved by having the azimuthal velocity decrease by a few tens of percent in tandem with the increase in radial inflow velocity. The large synthesized beam size ($0''.64 \times 0''.41$, $\text{PA} = 75.5^\circ$) precludes us from constructing a plot of $\Delta\theta'_{\text{sys}}(y')$ showing what would presumably be large twists at small radii (cf. Figure 3, which was made assuming a beam size of $0''.1$).

At the smallest velocities/largest radii, there appears in Figure 8 to be a constant offset in

$\Delta\theta'_{\text{wing}}$ of about 6 degrees. The offset may be due to a systematic error in the position angle we assumed for the outer disk. Another source of error at these low velocities may be in our systemic velocity (see Hughes et al. 2011 for a method to quantify this uncertainty).

To summarize, our first-cut analysis of the Casassus et al. (2013) ALMA observations of the HD 142527 disk demonstrates that the predicted spatio-kinematic signatures of fast radial inflow are eminently detectable, and merits a dedicated pursuit of inflow in a general sample of transition disks. Additional observations and modeling are posited to distinguish between a fast inflow or warp origin for the observed kinematics. This particular disk is especially challenging to interpret because of its complex and non-axisymmetric structures (Fukagawa et al. 2006; Fujiwara et al. 2006; Verhoeff et al. 2011; Casassus et al. 2012; Honda et al. 2012; Rameau et al. 2012; Casassus et al. 2013; Canovas et al. 2013). The disk interior to $R \sim 30$ AU that was inferred by Verhoeff et al. (2011) could, in principle, support a warp. Observations of an optically thin line that resolve the central cavity would help clarify the situation, to confirm the lower gas surface densities that should accompany fast inflow. Indeed, a recent study of the ^{13}CO and C^{18}O $J=3-2$ lines in this disk by Fukagawa et al. (2013) support the inflow scenario: they detect little (if any) emission from these optically thin isotopologues inside the disk cavity. No evidence for twisted isophotes or wing rotation is noted by Fukagawa et al. (2013) in these lines, but that is not surprising, as the emission is too faint — the current S/N is too low — inside the cavity region to detect these features.

4. CONCLUSIONS

Radial inflow of gas at velocities approaching free fall can account for both the depleted densities inside transition disk cavities and the relatively normal stellar accretion rates they maintain. We have demonstrated that high spatial and spectral resolution observations of molecular emission lines with (sub)millimeter wavelength interferometers — particularly ALMA — can detect inflow by virtue of its two key signatures: twisted isophotes at the systemic velocity, and rotated emission patterns in channel maps made in the line wings. We developed quantitative diagnostics of channel maps to characterize radial inflow, and discussed various real-world complications. Of these, the most serious is a warp.

We tested our inflow diagnostics on archival ALMA observations of the HD 142527 transition disk, uncovering a booming signal consistent with free-fall inflow velocities at distances of $\sim 25-50$ AU from the host star. Nevertheless a warped disk at these radii can also reproduce the large, order-unity rotations seen in the CO and HCO^+ line wings. Whether the HD 142527 disk cavity contains a fast radial inflow or a warped disk (or both), the only mechanism on the table now that can explain either phenomenon involves strong gravitational torques, exerted by one or more giant planets/brown dwarfs/low-mass stars (as yet undetected; see Biller et al. 2012; Casassus et al. 2013). Fast flows should also produce strong shocks in disks. We have not investigated the signatures of such shocks; the observables depend on details such as the density and the cooling mechanisms of shocked material. In the central cavity of the circumbinary disk around GG Tau A,

Beck et al. (2012) have detected hot H₂ that may trace shocks internal to the accretion flow.

We thank Ruobing Dong, Eve Lee, and Scott Tremaine for discussions, and the organizers of the 2013 Gordon Conference on Origins of Solar Systems, Ed Young and Fred Ciesla, for providing a great venue for sparking collaboration on this article. We also thank the referee Takayuki Muto for many insightful comments. This paper uses the following ALMA data: ADS/JAO.ALMA#2011.0.00465.S. ALMA is a partnership of ESO (representing its member states), NSF (USA) and NINS (Japan), together with NRC (Canada) and NSC and ASIAA (Taiwan), in cooperation with the Republic of Chile. The Joint ALMA Observatory is operated by ESO, AUI/NRAO and NAOJ. The National Radio Astronomy Observatory is a facility of the National Science Foundation operated under cooperative agreement by Associated Universities, Inc.

REFERENCES

- Alcalá, J. M., Natta, A., Manara, C. F., Spezzi, L., Stelzer, B., Frasca, A., Biazzo, K., Covino, E., Randich, S., Rigliaco, E., Testi, L., Comerón, F., Cupani, G., & D’Elia, V. 2013, ArXiv e-prints
- Andrews, S. M., Rosenfeld, K. A., Wilner, D. J., & Bremer, M. 2011, *ApJ*, 742, L5
- Augereau, J. C., Lagrange, A. M., Mouillet, D., Papaloizou, J. C. B., & Grorod, P. A. 1999, *A&A*, 348, 557
- Bast, J. E., Brown, J. M., Herczeg, G. J., van Dishoeck, E. F., & Pontoppidan, K. M. 2011, *A&A*, 527, A119
- Beck, T. L., Bary, J. S., Dutrey, A., Piétu, V., Guilloteau, S., Lubow, S. H., & Simon, M. 2012, *ApJ*, 754, 72
- Beckwith, S. V. W. & Sargent, A. I. 1993, *ApJ*, 402, 280
- Biller, B., Lacour, S., Juhász, A., Benisty, M., Chauvin, G., Olofsson, J., Pott, J.-U., Müller, A., Sicilia-Aguilar, A., Bonnefoy, M., Tuthill, P., Thebault, P., Henning, T., & Crida, A. 2012, *ApJ*, 753, L38
- Binney, J., Gerhard, O. E., Stark, A. A., Bally, J., & Uchida, K. I. 1991, *MNRAS*, 252, 210
- Brinch, C., Crapsi, A., Jørgensen, J. K., Hogerheijde, M. R., & Hill, T. 2007, *A&A*, 475, 915
- Brinch, C. & Hogerheijde, M. R. 2010, *A&A*, 523, A25
- Brinch, C., Hogerheijde, M. R., & Richling, S. 2008, *A&A*, 489, 607
- Brown, J. M., Blake, G. A., Qi, C., Dullemond, C. P., Wilner, D. J., & Williams, J. P. 2009, *ApJ*, 704, 496

- Bruderer, S. 2013, ArXiv e-prints
- Calvet, N., D’Alessio, P., Hartmann, L., Wilner, D., Walsh, A., & Sitko, M. 2002, *ApJ*, 568, 1008
- Calvet, N., D’Alessio, P., Watson, D. M., Franco-Hernández, R., Furlan, E., Green, J., Sutter, P. M., Forrest, W. J., Hartmann, L., Uchida, K. I., Keller, L. D., Sargent, B., Najita, J., Herter, T. L., Barry, D. J., & Hall, P. 2005, *ApJ*, 630, L185
- Canovas, H., Ménard, F., Hales, A., Jordán, A., Schreiber, M. R., Casassus, S., Gledhill, T. M., & Pinte, C. 2013, *A&A*, 556, A123
- Casassus, S., Perez M., S., Jordán, A., Ménard, F., Cuadra, J., Schreiber, M. R., Hales, A. S., & Ercolano, B. 2012, *ApJ*, 754, L31
- Casassus, S., van der Plas, G., M, S. P., Dent, W. R. F., Fomalont, E., Hagelberg, J., Hales, A., Jordán, A., Mawet, D., Ménard, F., Wootten, A., Wilner, D., Hughes, A. M., Schreiber, M. R., Girard, J. H., Ercolano, B., Canovas, H., Román, P. E., & Salinas, V. 2013, *Nature*, 493, 191
- Chang, P., Murray-Clay, R., Chiang, E., & Quataert, E. 2007, *ApJ*, 668, 236
- Crida, A., Morbidelli, A., & Masset, F. 2006, *Icarus*, 181, 587
- Curran, R. L., Argiroffi, C., Sacco, G. G., Orlando, S., Peres, G., Reale, F., & Maggio, A. 2011, *A&A*, 526, A104
- Dartois, E., Dutrey, A., & Guilloteau, S. 2003, *A&A*, 399, 773
- Dawson, R. I., Murray-Clay, R. A., & Fabrycky, D. C. 2011, *ApJ*, 743, L17
- de Gregorio-Monsalvo, I., Ménard, F., Dent, W., Pinte, C., López, C., Klaassen, P., Hales, A., Cortés, P., Rawlings, M. G., Tachihara, K., Testi, L., Takahashi, S., Chapillon, E., Mathews, G., Juhasz, A., Akiyama, E., Higuchi, A. E., Saito, M., Nyman, L.-Å., Phillips, N., Rodú, J., Corder, S., & Van Kempen, T. 2013, ArXiv e-prints
- De Marchi, G., Panagia, N., & Romaniello, M. 2010, *ApJ*, 715, 1
- Dodson-Robinson, S. E. & Salyk, C. 2011, *ApJ*, 738, 131
- Dong, R., Hashimoto, J., Rafikov, R., Zhu, Z., Whitney, B., Kudo, T., Muto, T., Brandt, T., McClure, M. K., Wisniewski, J., Abe, L., Brandner, W., Carson, J., Egner, S., Feldt, M., Goto, M., Grady, C., Guyon, O., Hayano, Y., Hayashi, M., Hayashi, S., Henning, T., Hodapp, K. W., Ishii, M., Iye, M., Janson, M., Kandori, R., Knapp, G. R., Kusakabe, N., Kuzuhara, M., Kwon, J., Matsuo, T., McElwain, M., Miyama, S., Morino, J.-I., Moro-Martin, A., Nishimura, T., Pyo, T.-S., Serabyn, E., Suto, H., Suzuki, R., Takami, M., Takato, N., Terada, H., Thalmann, C., Tomono, D., Turner, E., Watanabe, M., Yamada, T., Takami, H., Usuda, T., & Tamura, M. 2012, *ApJ*, 760, 111

- Dutrey, A., Guilloteau, S., Prato, L., Simon, M., Duvert, G., Schuster, K., & Menard, F. 1998, *A&A*, 338, L63
- Espaillat, C., Ingleby, L., Hernández, J., Furlan, E., D’Alessio, P., Calvet, N., Andrews, S., Muzerolle, J., Qi, C., & Wilner, D. 2012, *ApJ*, 747, 103
- Fujiwara, H., Honda, M., Kataza, H., Yamashita, T., Onaka, T., Fukagawa, M., Okamoto, Y. K., Miyata, T., Sako, S., Fujiyoshi, T., & Sakon, I. 2006, *ApJ*, 644, L133
- Fukagawa, M., Tamura, M., Itoh, Y., Kudo, T., Imaeda, Y., Oasa, Y., Hayashi, S. S., & Hayashi, M. 2006, *ApJ*, 636, L153
- Fukagawa, M., Tsukagoshi, T., Momose, M., Saigo, K., Ohashi, N., Kitamura, Y., Inutsuka, S.-i., Muto, T., Nomura, H., Takeuchi, T., Kobayashi, H., Hanawa, T., Akiyama, E., Honda, M., Fujiwara, H., Kataoka, A., Takahashi, S. Z., & Shibai, H. 2013, *ArXiv e-prints*
- Fung, J., Shi, J.-M., & Chiang, E. 2013, *ApJ*, submitted
- Garcia Lopez, R., Natta, A., Testi, L., & Habart, E. 2006, *A&A*, 459, 837
- Geers, V. C., Pontoppidan, K. M., van Dishoeck, E. F., Dullemond, C. P., Augereau, J.-C., Merín, B., Oliveira, I., & Pel, J. W. 2007, *A&A*, 469, L35
- Goldreich, P. & Tremaine, S. 1980, *ApJ*, 241, 425
- Goodman, J. & Rafikov, R. R. 2001, *ApJ*, 552, 793
- Guilloteau, S. & Dutrey, A. 1998, *A&A*, 339, 467
- Gullbring, E., Hartmann, L., Briceno, C., & Calvet, N. 1998, *ApJ*, 492, 323
- Honda, M., Maaskant, K., Okamoto, Y. K., Kataza, H., Fukagawa, M., Waters, L. B. F. M., Dominik, C., Tielens, A. G. G. M., Mulders, G. D., Min, M., Yamashita, T., Fujiyoshi, T., Miyata, T., Sako, S., Sakon, I., Fujiwara, H., & Onaka, T. 2012, *ApJ*, 752, 143
- Hopkins, P. F. & Quataert, E. 2011, *MNRAS*, 415, 1027
- Hughes, A. M., Andrews, S. M., Espaillat, C., Wilner, D. J., Calvet, N., D’Alessio, P., Qi, C., Williams, J. P., & Hogerheijde, M. R. 2009, *ApJ*, 698, 131
- Hughes, A. M., Wilner, D. J., Andrews, S. M., Qi, C., & Hogerheijde, M. R. 2011, *ApJ*, 727, 85
- Hughes, A. M., Wilner, D. J., Calvet, N., D’Alessio, P., Claussen, M. J., & Hogerheijde, M. R. 2007, *ApJ*, 664, 536
- Ireland, M. J. & Kraus, A. L. 2008, *ApJ*, 678, L59
- Isella, A., Pérez, L. M., & Carpenter, J. M. 2012, *ApJ*, 747, 136

- Kim, K. H., Watson, D. M., Manoj, P., Forrest, W. J., Najita, J., Furlan, E., Sargent, B., Espaillat, C., Muzerolle, J., Megeath, S. T., Calvet, N., Green, J. D., & Arnold, L. 2013, *ApJ*, 769, 149
- Klaassen, P. D., Juhasz, A., Mathews, G. S., Mottram, J. C., De Gregorio-Monsalvo, I., van Dishoeck, E. F., Takahashi, S., Akiyama, E., Chapillon, E., Espada, D., Hales, A., Hogerheijde, M. R., Rawlings, M., Schmalzl, M., & Testi, L. 2013, *A&A*, 555, A73
- Kraus, A. L. & Ireland, M. J. 2012, *ApJ*, 745, 5
- Larwood, J. D. 1997, *MNRAS*, 290, 490
- Lubow, S. H. & D’Angelo, G. 2006, *ApJ*, 641, 526
- Lynden-Bell, D. & Pringle, J. E. 1974, *MNRAS*, 168, 603
- Marzari, F. & Nelson, A. F. 2009, *ApJ*, 705, 1575
- Muzerolle, J., Calvet, N., Briceño, C., Hartmann, L., & Hillenbrand, L. 2000, *ApJ*, 535, L47
- Najita, J. R., Strom, S. E., & Muzerolle, J. 2007, *MNRAS*, 378, 369
- Ohashi, N. 2008, *Ap&SS*, 313, 101
- Omodaka, T., Kitamura, Y., & Kawazoe, E. 1992, *ApJ*, 396, L87
- Paczynski, B. 1977, *ApJ*, 216, 822
- Pavlyuchenkov, Y., Semenov, D., Henning, T., Guilloteau, S., Piétu, V., Launhardt, R., & Dutrey, A. 2007, *ApJ*, 669, 1262
- Piétu, V., Guilloteau, S., & Dutrey, A. 2005, *A&A*, 443, 945
- Pontoppidan, K. M., Blake, G. A., & Smette, A. 2011, *ApJ*, 733, 84
- Rameau, J., Chauvin, G., Lagrange, A.-M., Thébault, P., Milli, J., Girard, J. H., & Bonnefoy, M. 2012, *A&A*, 546, A24
- Reid, M. J., Schneps, M. H., Moran, J. M., Gwinn, C. R., Genzel, R., Downes, D., & Roennaeng, B. 1988, *ApJ*, 330, 809
- Rigliaco, E., Natta, A., Testi, L., Randich, S., Alcalà, J. M., Covino, E., & Stelzer, B. 2012, *A&A*, 548, A56
- Rosenfeld, K. A., Andrews, S. M., Hughes, A. M., Wilner, D. J., & Qi, C. 2013, *ApJ*, 774, 16
- Rosenfeld, K. A., Qi, C., Andrews, S. M., Wilner, D. J., Corder, S. A., Dullemond, C. P., Lin, S.-Y., Hughes, A. M., D’Alessio, P., & Ho, P. T. P. 2012, *ApJ*, 757, 129

- Schwarz, M. P. 1981, *ApJ*, 247, 77
- Semenov, D., Pavlyuchenkov, Y., Henning, T., Wolf, S., & Launhardt, R. 2008, *ApJ*, 673, L195
- Shlosman, I., Frank, J., & Begelman, M. C. 1989, *Nature*, 338, 45
- Sicilia-Aguilar, A., Henning, T., & Hartmann, L. W. 2010, *ApJ*, 710, 597
- Stahler, S. W., Korycansky, D. G., Brothers, M. J., & Touma, J. 1994, *ApJ*, 431, 341
- Tang, Y.-W., Guilloteau, S., Piétu, V., Dutrey, A., Ohashi, N., & Ho, P. T. P. 2012, *A&A*, 547, A84
- Thalmann, C., Grady, C. A., Goto, M., Wisniewski, J. P., Janson, M., Henning, T., Fukagawa, M., Honda, M., Mulders, G. D., Min, M., Moro-Martín, A., McElwain, M. W., Hodapp, K. W., Carson, J., Abe, L., Brandner, W., Egner, S., Feldt, M., Fukue, T., Golota, T., Guyon, O., Hashimoto, J., Hayano, Y., Hayashi, M., Hayashi, S., Ishii, M., Kandori, R., Knapp, G. R., Kudo, T., Kusakabe, N., Kuzuhara, M., Matsuo, T., Miyama, S., Morino, J.-I., Nishimura, T., Pyo, T.-S., Serabyn, E., Shibai, H., Suto, H., Suzuki, R., Takami, M., Takato, N., Terada, H., Tomono, D., Turner, E. L., Watanabe, M., Yamada, T., Takami, H., Usuda, T., & Tamura, M. 2010, *ApJ*, 718, L87
- van der Marel, N., van Dishoeck, E. F., Bruderer, S., Birnstiel, T., Pinilla, P., Dullemond, C. P., van Kempen, T. A., Schmalzl, M., Brown, J. M., Herczeg, G. J., Mathews, G. S., & Geers, V. 2013, *Science*, 340, 1199
- van Zadelhoff, G.-J., van Dishoeck, E. F., Thi, W.-F., & Blake, G. A. 2001, *A&A*, 377, 566
- Verhoeff, A. P., Min, M., Pantin, E., Waters, L. B. F. M., Tielens, A. G. G. M., Honda, M., Fujiwara, H., Bouwman, J., van Boekel, R., Dougherty, S. M., de Koter, A., Dominik, C., & Mulders, G. D. 2011, *A&A*, 528, A91
- Weinberger, A. J., Becklin, E. E., Schneider, G., Smith, B. A., Lowrance, P. J., Silverstone, M. D., Zuckerman, B., & Terrile, R. J. 1999, *ApJ*, 525, L53
- Yorke, H. W. & Bodenheimer, P. 1999, *ApJ*, 525, 330
- Zhu, Z., Nelson, R. P., Hartmann, L., Espaillat, C., & Calvet, N. 2011, *ApJ*, 729, 47